View metadata, citation and similar papers at core.ac.uk
brought to you by CORE
provided by Helsingin yliopiston digitaalinen arkisto

Magnetic properties and resistive switching in mixture films and nanolaminates consisting of iron and silicon oxides grown by atomic layer deposition

Running title: Iron silicon oxide films grown by atomic layer deposition

Running authors: Kukli *et al*.

Kaupo Kukli,[1,*] Marianna Kemell,[1] Helena Castán,[3] Salvador Dueñas,[3] Joosep Link,[4] Raivo Stern,[4] Mikko J. Heikkilä,[1] Taivo Jõgiaas,[2] Jekaterina Kozlova,[2] Mihkel Rähn,[2] Kenichiro Mizohata,[5] Mikko Ritala,[1] Markku Leskelä[1]

[1]Department of Chemistry, University of Helsinki, P.O. Box 55, FI-00014 Helsinki, Finland

[2]Institute of Physics, University of Tartu, W. Ostwald 1, 50411 Tartu, Estonia

[3]Department of Electronics, University of Valladolid, Paseo Belén, 15, 47011 Valladolid, Spain

[4]National Institute of Chemical Physics and Biophysics, Akadeemia tee 23, EE-12618 Tallinn, Estonia

[5]Accelerator Laboratory, Department of Physics, University of Helsinki, P.O. Box 43, FI-00014 Helsinki, Finland

* Current address: Institute of Physics, University of Tartu, W. Ostwald 1, 50411 Tartu, Estonia; e-mail: kaupo.kukli@ut.ee

SiO_2-Fe_2O_3 mixture films and nanolaminates were grown by atomic layer deposition from iron trichloride, hexakis(ethylamino)disilane, and ozone at 300 ^oC. Orthorhombic ε-Fe_2O_3 was identified in Fe_2O_3 reference films, and in Fe_2O_3 layers grown to certain thicknesses between amorphous SiO_2 layers. SiO_2-Fe_2O_3 films could be magnetized in external fields, exhibiting saturation and hysteresis in nonlinear magnetization-field curves. Electrical resistive switching, markedly dependent on the ratio of the component oxides, was also observed in films with proper composition. For relatively conductive films, application of small signal measurements allowed one to record memory maps with notable squareness and defined distinction between high and low conductance states.

Keywords: atomic layer deposition, iron oxide, silicon oxide, nanocomposite, multilayers, nanolaminates, magnetic materials, resistive switching

I. INTRODUCTION

Multilayers, superlattices, and nanolaminates consisting of different metal oxides are attractive for many applications ranging from optical filters to mechanically resistant coatings. Multilayering chemically and structurally distinctive materials may allow one to tailor physical properties characteristic of component layers. For instance, electrically or magnetically functional nanomaterials can be combined and the degree of their structural ordering controlled in periodical stacks with mechanical constraints or electronic charge barriers. Henceforth, one could simultaneously modify growth of magnetic nanocrystalline materials and improve insulating properties in the composites. In this regard, one can propose,

that nanolaminate structures consisting of oxides of silicon and iron enable materials demonstrating saturative magnetization in a medium exhibiting tunable insulating behavior.

Layered composites of amorphous SiO_2 and structurally ordered Fe_2O_3 particles containing hematite, α-Fe_2O_3, [1,2] maghemite, γ-Fe_2O_3, [3-5] and magnetite, Fe_3O_4, [6,7] as crystallographic phases have earlier been fabricated and studied in several works. In these composites, nonlinear magnetization of the solid media was achieved and recorded. It is also worth noting that, besides magnetic materials, also other, mostly catalytic, applications of powdered SiO_2-Fe_2O_3 composites have been found prospective, whereby the composites were prepared by sputtering,[8] hydrothermal synthesis,[9] and coevaporation of Si and Fe in an oxygen ambient.[10] The latter composites contained the hematite phase of Fe_2O_3 .

In regard with the behavior of single metal oxides as resistive switching media in electric fields, both SiO_2[11-14] and Fe_2O_3[15] have earlier been separately studied. Spintronic effects in Fe_2O_3 films became observable due to the current-induced magnetic ordering followed by decreased scattering of polarized electrons, allowing current-controlled low resistance state and and voltage-controlled high resistance state.[15] Demonstration of both tunable conductivity and magnetic polarization in as-deposited material layer of any particular compound should be of interest. Evaluation of resistive switching in SiO_2-Fe_2O_3 composites or layered stacks has not yet been specifically targeted, though. Some papers have, however, described performance of memristor-type devices comprising both SiO_2 and Fe_2O_3 films in double-layer structures.[16,17]

In a few studies earlier, electrical control of ferromagnetism has been addressed and, partially, described. Coexistence of nonlinear saturative magnetization and resistive switching has been observed in pulsed laser deposited HfO_2/Nb:$SrTiO_3$ based film,[18] in pulsed laser deposited TiO_2 film based structures,[19] and also in far more complex quaternary metal oxide layers prepared by wet chemistry and spin-coating.[20] In the latter case, the oxide films consisted partially of ferrite compounds. Very generally, iron oxide thin films may be considered as one of the natural choices for easily and remanently magnetizing media, but they have not been considered and exploited as insulating dielectrics. As was mentioned above, resistive switching in iron oxide based media has in a few cases been already reported.[15-17] The otherwise interesting phenomenon observed and described as multilevel switching in such films may have been, partially, caused also by internal heterogeneity of the iron oxide phase composition. Nevertheless, the exploitation of iron oxide in the form of both magnetizing and resistively switching material layers appears as an intriguing task, provided that the electrical leakage currents through iron oxide components can be reduced. In addition, application of chemical gas-phase deposition routes to homogeneous large-area thin films, in particular, atomic layer deposition (ALD) should be adapted, in order to conveniently enable multilayering of constituent compounds at moderate process temperatures.

ALD as a method generally suited to the growth of uniform thin films on arbitrarily shaped substrates can be applied for the growth of artificially structured multilayers composed of different oxides. SiO_2 films have earlier been grown by ALD from $Si_2(NHEt)_6$ and O_3[21] and studied as constituent in $AlSiO_x$ mixtures.[22] Growth of ε-Fe_2O_3 films by ALD from $FeCl_3$ and H_2O has also been reported earlier.[23]

In the present study, mixed films and nanolaminates of crystalline iron oxide and amorphous silicon oxide were grown by ALD from iron trichloride, $FeCl_3$, hexakis(ethylamino)disilane, i.e. $Si_2(NHEt)_6$, and ozone, O_3, precursors at a substrate temperature fixed at 300 ^oC. Magnetization in external magnetic fields as well as resistive switching behavior under electrical voltage pulses were separately examined in materials in their as-deposited state. The relative contents of iron and silicon oxides were modified in superlattice-like nanolaminate structures in order to initiate the crystal growth in the iron oxide constituent layers intensely enough to give rise to hysteretic magnetization. Concurrently, it was of interest to study, whether the combination of silicon oxide in the multilayers with leaky iron oxides could, lower the leakage currents at levels low enough to allow switching between high and low resistivity states under alternating sampling bias voltages.

II. EXPERIMENTAL

The films were grown in a commercial hot-wall flow-type F120 ALD reactor[24] (ASM Microchemistry, Ltd.). The iron oxide films were grown using $FeCl_3$, and silicon oxide films using hexakis(ethylamino)disilane, $Si_2(NHEt)_6$, also denoted as AHEAD (Air Liquide). Ozone was exploited as oxygen precursor. Ozone was produced with a Wedeco Ozomatic Modular 4 HC ozone generator from oxygen (99.999%, Linde Gas). The estimated ozone concentration output of the generator was about 100 g/m^3. $Si_2(NHEt)_6$ was evaporated at 65-67 ^oC and $FeCl_3$ at 145-150 ^oC. The growth temperature was held at 300 ^oC. The deposition cycle sequences for both Fe_2O_3 and SiO_2 were 2.0-1.0-2.0-1.0 s for cation precursor-purge-ozone-purge lengths.

The substrates were cut out of wafers of undoped Si(100) covered with a 1.5–2.0 nm thick wet-chemically-grown SiO_2. Electrically conducting substrates were also used, based on (100) silicon with a resistivity of 0.014–0.020 Ω·cm, i.e., Si boron-doped to the concentrations up to $5 \times 10^{18} - 1 \times 10^{19}/cm^3$, and coated with 10 nm thick titanium nitride layer. TiN had been chemical vapor deposited using $TiCl_4/NH_3$ process in an ASM A412 Large Batch 300 mm reactor at Fraunhofer IPMS-CNT. The SiO_2-Fe_2O_3 films were grown to thicknesses ranging from ca. 30 to 50 nm. The numbers of SiO_2 and Fe_2O_3 deposition cycles were varied separately in order to change the thicknesses of the constituent metal oxide layers and the Fe to Si ratio of the films. In this way, films having different artificial structures were deposited, ranging from those with SiO_2 doped or mixed in low amounts with Fe_2O_3 to SiO_2-Fe_2O_3 nanolaminates enabling growth of Fe_2O_3 nanocrystals. The growth cycle sequences applied for the different samples are presented in Table I.

Table I. List of Fe_2O_3-SiO_2 films grown to the thicknesses and possessing iron to silicon elemental ratios measured by energy dispersive X-ray spectrometry (EDX).

ALD growth cycle sequences	Thickness	Fe:Si ratio
$500 \times Fe_2O_3$; a reference iron oxide film	28 nm	
$250 \times Fe_2O_3 + 20 \times SiO_2 + 250 \times Fe_2O_3$	50 nm	11:1
$4 \times [100 \times Fe_2O_3 + 20 \times SiO_2] + 100 \times Fe_2O_3$	47 nm	5:1
$4 \times [75 \times Fe_2O_3 + 50 \times SiO_2] + 75 \times Fe_2O_3$	37 nm	2:1
$10 \times [25 \times Fe_2O_3 + 2 \times SiO_2] + 25 \times Fe_2O_3$	48 nm	6:1
$10 \times [25 \times SiO_2 + 4 \times Fe_2O_3] + 25 \times SiO_2$	44 nm	0.7:1

Energy dispersive X-ray spectrometry (EDX) was applied for the measurement of the relative iron and silicon contents by a Hitachi S-4800 scanning electron microscope (SEM) equipped with an Oxford INCA 350 EDX spectrometer. In order to avoid interference from the silicon

substrates while measuring the silicon content, all the samples were, in parallel, grown on pieces of silicon wafer and aluminum foil. The EDX spectra were measured at 20 keV frrom films deposited on the Al foil. The beam current and spectrometer gain were determined from a calibration measurement performed under the same beam conditions. The calculations were done on the basis of Fe K_α and Si K_α X-ray lines using a GMRFILM program.[25] Contents of residual light elements in selected samples were determined by time-of-flight elastic recoil detection analysis (TOF-ERDA).[26] The TOF-ERDA was performed with a 5 MV tandem accelerator using 50 MeV $^{127}I^{+}$ ion beam. For the film thickness calculations, the film densities were estimated based on the Fe:Si ratios.

The thicknesses of the films were evaluated either by X-ray reflectometry (XRR) or by EDX spectroscopy. XRR was performed using a PANalytical X'Pert Pro MPD X-ray diffractometer with Cu Kα source using a 1/16° divergence slit, Cu attenuator and parallel plate collimator slit. The density, thickness and roughness of the layers were acquired by fitting a theoretical model to the measured data using either Reflectivity 1.2 (PANalytical) or Reflex35[27] softwares. By using the same equipment, grazing incidence X-ray diffraction (GIXRD) analysis was carried out in order to determine the phases formed in the iron oxide layers, using CuKα radiation (1.5406 Å), 1/4° divergence slit and parallel beam optics. The reflection peaks were indexed and phases determined after Rietveld analysis using the program Profex (ver. 3.11.1).[28] Lamellae of selected nanolaminates on different substrates were prepared for transmission electron microscopy using FEI Helios Nanolab™ 600 DualBeam™ scanning microscope equipped with focused ion beam (FIB) module and Omniprobe model 100.7 in-situ nanomanipulator. High-resolution transmission electron microscopy (HRTEM) studies for the characterization of the cross-sections of the

nanolaminate structures were carried out using FEI Titan Themis 200 instrument with a field emission gun operated at 200 kV.

In order to carry out electrical measurements, metal-insulator-metal (MIM) type structures were prepared on the conducting substrates. Top electrodes with an area of 0.052 mm^2 were formed by electron beam evaporation of 120 nm thick Al/Ti dots through a shadow mask, with the Ti layer directly contacting the SiO_2–Fe_2O_3 nanolaminates. Admittance-voltage and current-voltage measurements were carried out in a light-proof and electrically shielded box. Samples were electrically characterized in both d.c. and a.c. regimes using a Keithley 4200SCS semiconductor analyzer. The bias voltage was applied to the top electrode, while the bottom electrode was grounded. To record the admittance parameters, a small signal of 30 mV r.m.s. was superimposed with the d.c. bias voltage. In accord with the observations, the experimental frequency did not affect the resistive switching behavior in the range of 20 kHz - 1 MHz. Magnetic measurements were performed using the Vibrating Sample Magnetometer (VSM) option of the Quantum Design 14 T Physical Property Measurement System by scanning the magnetic field from − 50000 to + 50000 Oe (from − 397.9 to + 397.9 kA/m) parallel to the film surface at 5 K and at room temperature.

III. RESULTS AND DISCUSSION

A. Structure and composition

XRR measurements were conducted on selected samples to examine whether the component oxide layers were distinctively deposited in the stacks. The measurements revealed that multilayer structures had feasibly been formed (Fig. 1). The relatively high maxima in the

pattern were unambiguosly characteristic of superlattice-like structures and indicative of sharp interfaces between the constituent material layers, whereas the distance between the shorter period oscillations was inversely proportional to the total nanolaminate thickness. In general, the period of the superlattice maxima becomes gradually longer or shorter as the bilayer thickness decreases or increases, respectively.[29-32] The measured patterns were in a good agreement with the simulations giving proof of not only a nanolaminate structure, but also of appreciable layer thickness uniformity (Fig. **1**).

The XRR patterns of SiO_2-Fe_2O_3 nanolaminates were satisfactorily fitted (Fig. **1**) using a model with four equal bilayers and a Fe_2O_3 top layer. A SiO_2 layer with a thickness of 1.9-2.2 nm and a roughness of 0.3-0.6 nm between the nanolaminate and the silicon substrate had to be taken into account in order to reach the satisfactory match between the measured and modeled curves.

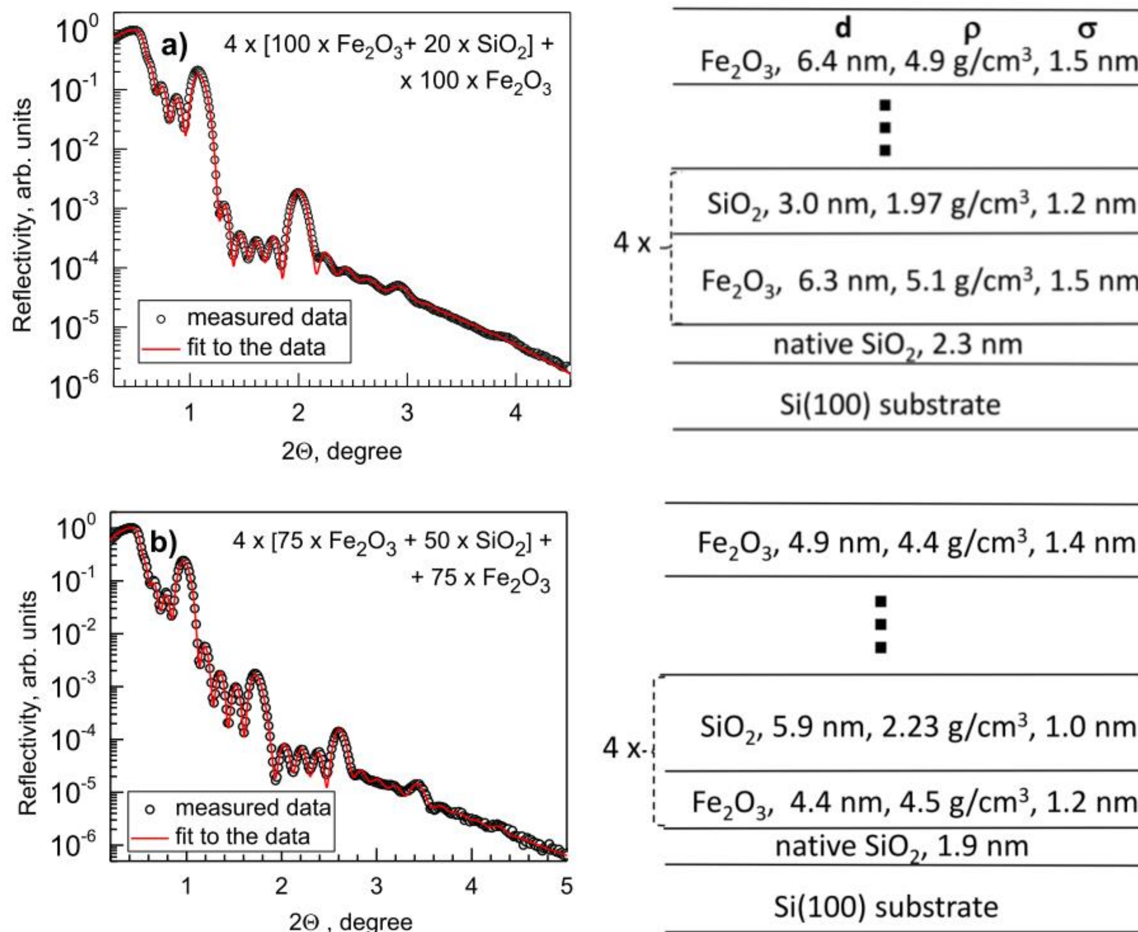

Figure 1. Measured and fitted X-ray reflection patterns from SiO_2-Fe_2O_3 nanolaminate film grown using ALD cycle sequences indicated by the labels (left column) and schematic representation of the nanolaminate structures with layer thicknesses, d, mass densities, ρ, and roughnesses, σ, as fitting results (right column). In both panels a) and b) of the left column, every other data point is omitted for the sake of clarity.

Selected nanolaminate films were analysed by TEM (Fig. 2). The TEM results visualized that the films indeed consisted of defined periodical multilayers. Nanolaminate structures were grown on all substrates: SiO_2/Si substrates (used in magnetic measurements), TiN/Si (used for electrical evaluation) and Al (used in EDX

measurements to enable the measurements of Si in the films). One can notice somewhat wavy and rough nature of the alternating layers and diffuse interfaces between the constituent oxides. This is most probably caused by the strong tendency of Fe_2O_3 to crystallize, which increases morphological nonuniformities. The roughness caused by the nanocrystalline nature of the iron oxide component is also reflected in XRR curves that are deformed at 2Θ angles higher than 3° (Fig. 1)

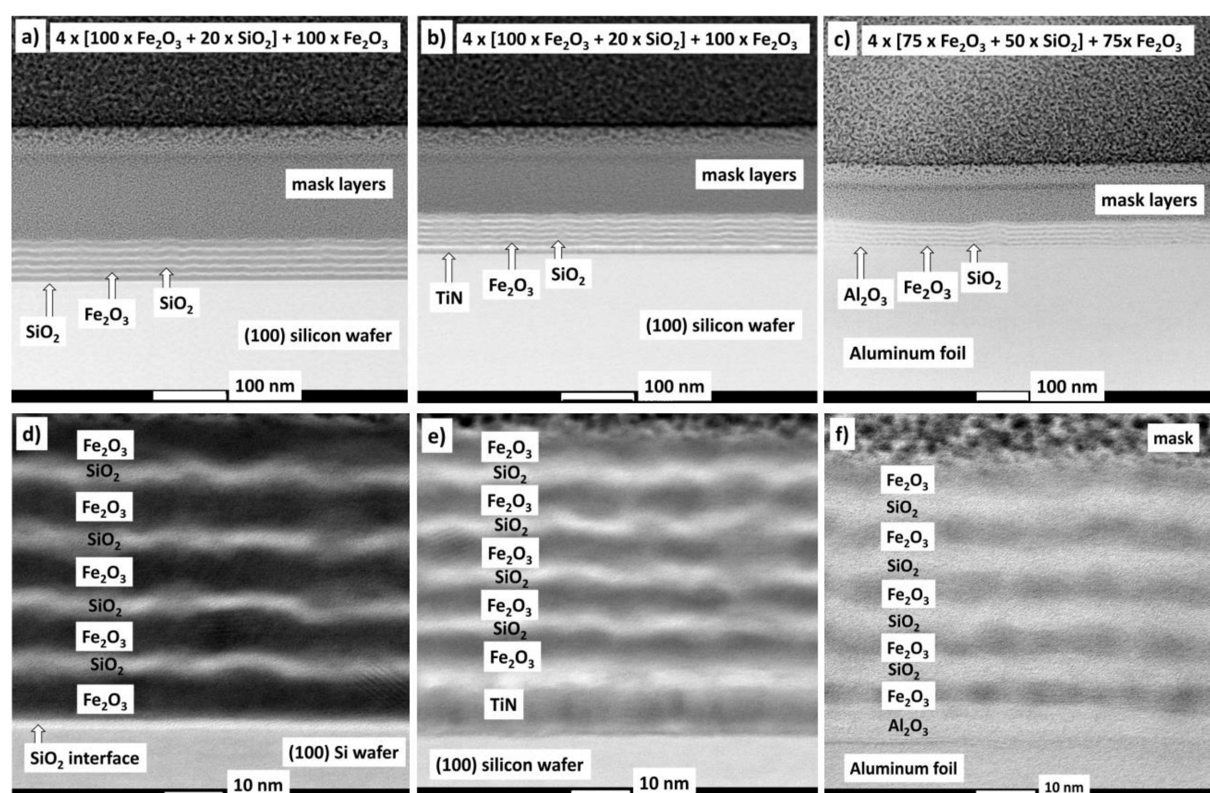

Figure 2. Transmission electron microscopy images of Fe_2O_3-SiO_2 nanolaminate films grown on SiO_2/Si substrates (a) and d)), Si substrates covered by a TiN layer (b) and e)), and aluminum foil (c) and f)). The corresponding growth cycle sequences are indicated on the panels in the upper row. The layers of distinct chemical composition constituting the film stacks are labeled correspondingly.

The Fe_2O_3 films grown in this study clearly started to crystallize in their as-deposited states (Fig. 3). The extent of crystallization and the phase composition was markedly influenced by the content of SiO_2 in the mixed or laminated films, as expected. It is to be noted, at first, that

most of the reflections in the diffractograms could be assigned as those of either the cubic maghemite (ICDD card 4-755) or rhombohedral hematite (ICDD card 33-664). Apparently, the crystallized part of the thin film material contained a mixture of iron oxide phases. However, the clear reflection peaks at 37 and 61 degrees did not match with any of the common phases, i.e. maghemite, magnetite, or hematite. At the same time, all the reflection peaks apparent in the diffractogram of 25-30 nm thick Fe_2O_3 film grown without SiO_2 additives could be attributed to the nanocrystalline orthorhombic ε-Fe_2O_3 (ICSD card 173024) (Fig. 3, a).

Further, in a triple-layer structure comprising two Fe_2O_3 films embedding a single very thin SiO_2 layer, the phase unambiguosly recognized was ε-Fe_2O_3 (Fig. 3, b), as concluded on the basis of diffraction peaks with somewhat lower intensity and larger width compared to those of the bare Fe_2O_3 film. Expectedly, insertion of even small amounts of SiO_2 into the host iron oxide decreased the intensity of crystallization in the as-deposited Fe_2O_3 films. The ε-Fe_2O_3 polymorph has earlier been obtained with the ALD process using $FeCl_3$ and H_2O as precursors.[23] It has also been stated that ε-Fe_2O_3 is an intermediate phase on the polymorphous route from γ -Fe_2O_3 to α-Fe_2O_3, and the ε-Fe_2O_3 exists only in the form of nanocrystalline material due to surface energy related factors.[33] Since ALD proceeds via gas-phase deposition forming layers with slowly and monotonously increasing thickness, stabilization of intermediate phases in their nanocrystalline form can indeed be expected.

The appearance of the ε-Fe_2O_3 phase in the composites and mixture films with silicon oxide has been observed also before. For instance, magnetic colloidal rod-shaped mesoporous particles have been made of silica (SiO_2) and iron oxide (ε-Fe_2O_3) using a solvent-free

melting impregnation method to form iron oxide nanocrystals inside silica nanopores.[34] ε-Fe_2O_3 nanoparticles have been formed by heat-treating amorphous Fe–Si–O films deposited by magnetron sputtering of $(\alpha\text{-}Fe_2O_3)_{1-x}(SiO_2)_x$ composites.[35] Furthermore, ε-Fe_2O_3 has also been formed by implantation of iron oxide particles in SiO_2 glass,[36] or impregnation of mesoporous silica matrix by iron nitrate.[37]

To examine the stability of the polymorphs and distinction between the different phases, that is γ -Fe_2O_3 (maghemite), ε-Fe_2O_3, and α-Fe_2O_3 (hematite), selected films were heated in air at 800 ^{o}C. Expectedly, the ε-Fe_2O_3 was turned into the hematite phase, that is clearly distinguishable from the orthorhombic polymorph ε-Fe_2O_3 (Fig. **3**, c).

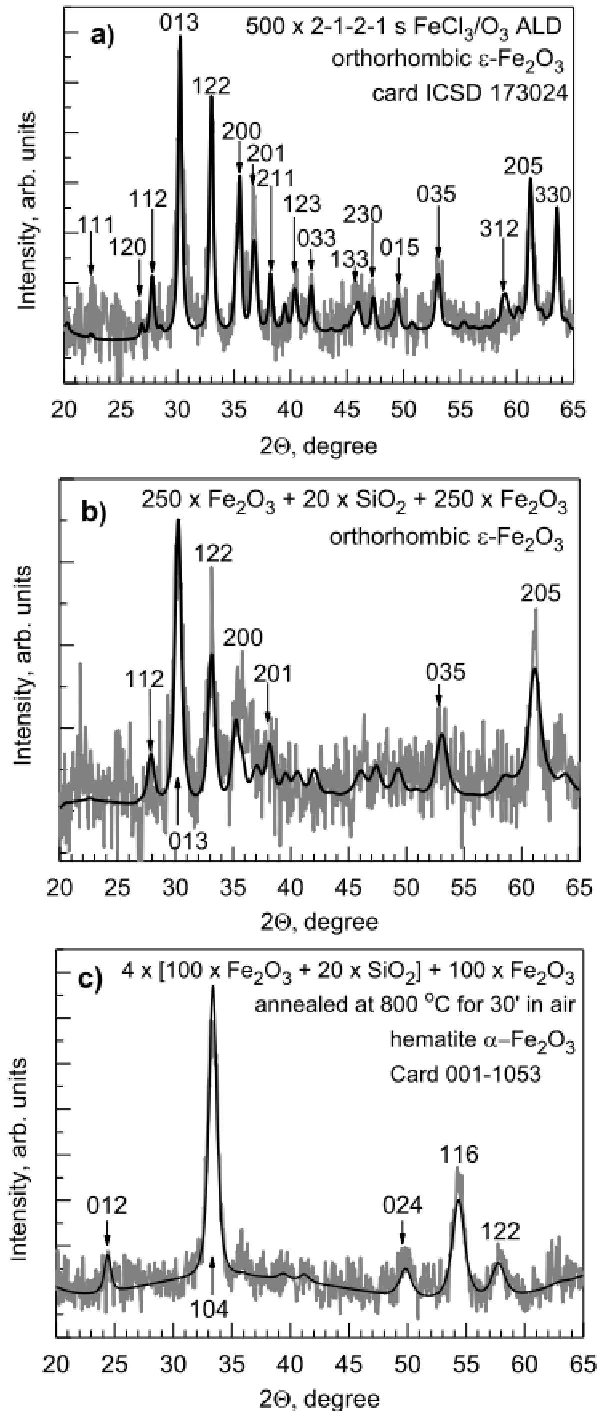

Figure 3. Grazing incidence X-ray diffractograms from a) 28 nm thick Fe_2O_3 film, b) 50 nm thick Fe_2O_3 film embedding a 2-3 nm thick SiO_2 interlayer, and c) a nanolaminate film after annealing at 800 ºC in air. Experimental and fitted difractograms are represented by bold gray and solid black curves, respectively. Reflexes above the noise level are designated as those belonging to the Fe_2O_3 polymorphs and indicated by the corresponding labels for the epsilon-phase in top and middle panels and hematite in bottom panel.

In the Fe_2O_3-SiO_2 films consisting of relatively thinner composite layers, the crystal growth of iron oxide became naturally restricted, as revealed by the XRD. Fig. 4 depicts diffractograms measured from Fe_2O_3-SiO_2 nanolaminates and mixture films with increasing relative silicon content. In these structures certain, although weak, crystallographic ordering was still observable, owing to the onset of crystallization in the thin, but chemically still distinct, iron oxide layers. In such cases the ambiguity of the phase determination increased. However, the reflections apparent in the diffractograms could still be assigned as those characteristic of ε-Fe_2O_3 (Fig. 4) One can also presume that the probability of the formation of metastable crystalline oxide polymorphs increases with the decrease in the layer thickness of these oxides. Thus, the assignment of the XRD patterns to ε-Fe_2O_3 (Fig. 4) becomes justified.

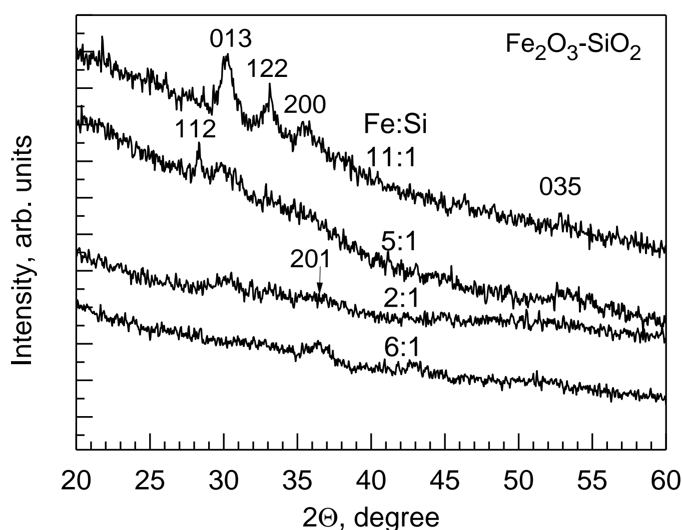

Figure 4. Grazing incidence X-ray diffractograms from as-deposited Fe_2O_3 films mixed or laminated with SiO_2 with molar Fe:Si ratios (EDX), indicated by the labels. For the description of the growth cycle sequences, see Table **I**

Figure 5 represents scanning electron microscope images of the surfaces of the as-deposited Fe_2O_3-SiO_2 films. One can see, that the surface of a 28 nm thick Fe_2O_3 film, not mixed with SiO_2, consists of uniform features which may well characterize a polycrystalline material with

grain boundaries developed up to the very surface and thus clearly visible. A decrease in the thickness of the topmost Fe_2O_3 layer in the nanolaminates apparently caused a slight decrease in the grain size on the surface. However, the XRR results (Fig. 1) did not reveal any significant differences in the roughness of the top layers of the laminate structures. At the same time, the average grain size, as estimated from the SEM images, also decreased along with the increase in the number of intermediate SiO_2 growth cycles. Surfaces of the films where the topmost layer was amorphous SiO_2 (Fig. 5) remained, expectedly, relatively featureless and smoother compared to the multilayers terminated by iron oxide.

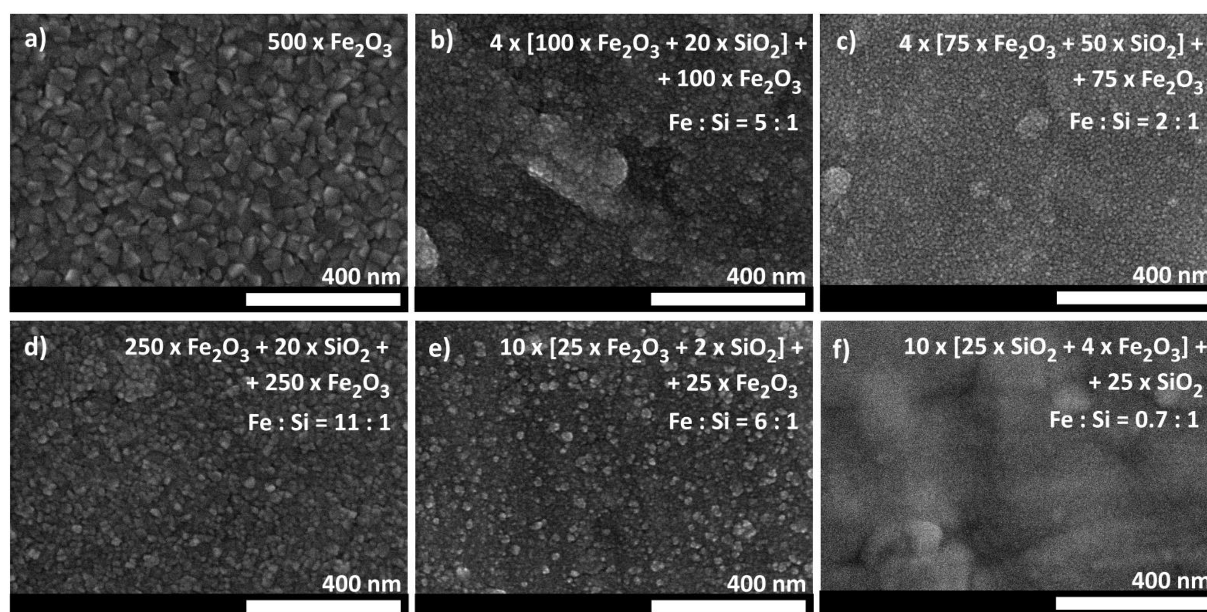

Figure 5. Scanning electron microscopy images from the surfaces of Fe_2O_3-SiO_2 films as-deposited using cycle sequences indicated by the labels.

Selected samples were evaluated by ToF-ERDA in order to determine contents of light residual elements averaged throughout the film thicknesses. The triple layer grown using the ALD cycle sequence of 250 $\times$ Fe_2O_3 + 20 $\times$ SiO_2 + 250 $\times$ Fe_2O_3 consisted of 37.8 $\pm$ 0.4 at.% Fe, 60.0 $\pm$ 0.6 at.% O, and 1.6 $\pm$ 0.4 at.% Si. The contents of residual impurities were measured as low as 0.27 $\pm$ 0.04 at.% chlorine, 0.18 $\pm$ 0.04 at.% nitrogen, 0.18 $\pm$ 0.04 at.% carbon, and 0.44 $\pm$ 0.12 at.% hydrogen.

The nanolaminate grown on TiN using the ALD cycle sequence of $4 \times [100 \times Fe_2O_3 + 20 \times SiO_2] + 100 \times Fe_2O_3$ consisted of 23.2 ± 0.3 at.% Fe, 52.6 ± 0.5 at.% O, and 5.5 ± 0.5 at.% Si. The residual impurities were detected as 0.39 ± 0.04 at.% Cl, 7.9 ± 0.2 at.% N, 0.26 ± 0.02 at.% C, and 0.74 ± 0.12 at.% H. In this stack of the films grown on TiN-covered silicon substrate, the contribution from the TiN electrode layer to the composition was as high as 9.4 ± 0.2 at.% Ti which also explains the high nitrogen content detected in the film.

ToF-ERDA on the film which exhibited the most well defined resistive switching behavior, i.e. the film grown using the sequence of $4 \times [75 \times Fe_2O_3 + 50 \times SiO_2] + 75 \times Fe_2O_3$] (Fig. 8) revealed, that the film contained 18.7 ± 0.3 at.% Fe, 61.8 ± 1.7 at.% O, and 9.90 ± 1.3 at.% Si. The contents of residual impurities were 2.10 ± 0.17 at.% chlorine, 0.76 ± 0.20 at.% nitrogen, 0.40 ± 0.22 at.% carbon, and 5.8 ± 2.8 at.% hydrogen.

The ToF-ERDA results indicated that the impurity contents were appreciably low in the as-deposited laminate films. The presence of such impurities is, nevertheless, to be taken into account, as they naturally affect the structure and performance of magnetic and electric films by increasing the defect densities. However, to improve the electrical performance of the SiO_2-Fe_2O_3 films, the presence of silicon and iron oxides in comparable amounts or at least in contents of the same order of magnitude seem to be necessary in multilayers.

B. Magnetic behavior

Figure 6 depicts magnetization curves measured for selected samples in external magnetic field at room temperature. One can see, that the magnetization in the SiO_2-Fe_2O_3 films was easy, proceeding nonlinearly against the external field, and tended to saturate at sufficiently high fields exceeding 5000-10000 Oe applied in the plane of the film surface. Hysteresis in the magnetization-field loops remained rather narrow and the coercive field was thus weak. Analogous behavior in some iron oxide-silicon oxide composites has been observed earlier.[34, 38] In the present study, the magnetization-field curves measured from the films grown using cycle sequences of 4 × [75 × Fe_2O_3 + 50 × SiO_2] + 75 × Fe_2O_3 (Fig. 6) 4 and × [100 × Fe_2O_3 + 20 × SiO_2] + 100 × Fe_2O_3 (not shown), displayed insignificant coercive fields at room temperature and saturation magnetization did not exceed 2.5×10^{-4} and 2.5×10^{-5} emu/g, respectively. At low temperature, i.e. at 5 K, the coercivity increased noticeably up to 1.2 kOe (not shown) and 4.6 kOe (Fig. 7), respectively, whereas the saturation magnetization values remained in the same order of magnitude as in the high-temperature measurements.

In accord with the literature, the orthorhombic ε-Fe_2O_3 has emerged as possibly the most interesting phase of iron oxide, mainly due to its ferromagnetic performance with remarkable coercive field at low and room temperatures, as well as magnetoelectric properties.[38-46] As already noted, the ε-Fe_2O_3 has been recognized as a metastable phase of iron oxide, which can be achieved only in nanocrystalline material upon polymorphous transformation between maghemite (γ-Fe_2O_3) and hematite (α-Fe_2O_3) phases.[33,47-49] Magnetic ε-Fe_2O_3 nanoparticles have earlier been prepared often by wet chemical synthesis. [38,44,45,50,51]

In the present study, the magnetic behavior of the triple Fe_2O_3-SiO_2-Fe_2O_3 layer, in which the content of ε-Fe_2O_3 was significant (Fig. 2), resembles that observed by Li *et al.* [34] In the latter work, iron oxide nanocrystals were stabilized within spaces confined inside mesoporous silica after annealing in order to crystallize the ε-Fe_2O_3 phase, and the coercivities were in the range of 2000-2500 Oe, as measured below room temperature, i.e. at 200 K. It is also worth noting that in another work by Kubíčková et al. [37], devoted to the investigations of the properties of homogeneously mixed SiO_2-Fe_2O_3suspensions, the magnetic coercivities measured at 300 K were decreased down to zero, whereas the coercivity of reference ε-Fe_2O_3 sample without SiO_2 extended to 20 kOe in the same study.

One could notice certain deformation of the magnetization-field loop measured on the triple Fe_2O_3-SiO_2-Fe_2O_3 layer (Fig. 6, lower panel). When reaching zero fields during sweeping the external field strength, the response of the magnetization intensifies, even indicating a tendency to discontinuous response to the field and a „kink" like feature close to the zero field. Such a kink in the magnetization curve near the zero field has been proposed to be indicative of the presence of ferrimagnetic γ-Fe_2O_3 polymorph impurities.[45] It is worth noting, that analogous tendencies in the development of such abrupt kinks have been observed in several works,[34, 38, 40, 41, 44] although structural analyses have not always revealed multiphase structure.

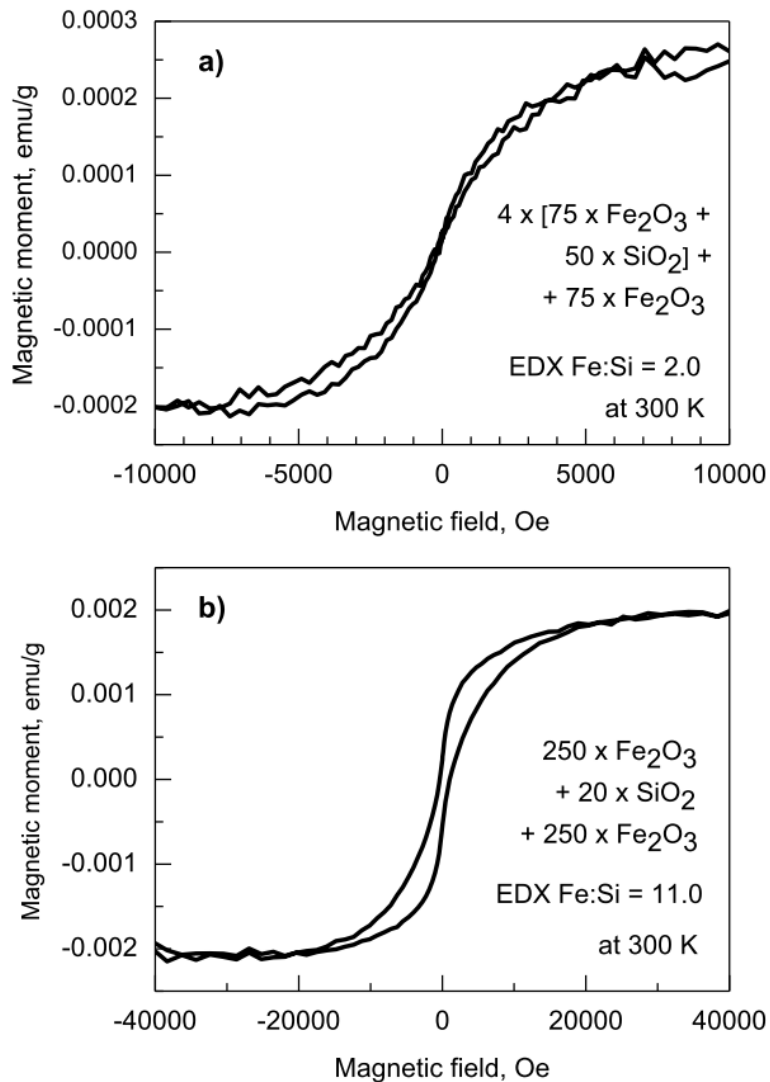

Figure *6*. Room-temperature magnetization curves measured from periodical Fe_2O_3-SiO_2 nanolaminate (upper panel) and Fe_2O_3-SiO_2-Fe_2O_3 triple layer (lower panel) grown using ALD cycle sequences and with Fe:Si atomic ratio described by the labels.

Figure 7 depicts magnetization-field loops measured from selected samples at a low temperature, 5 K. One can see again, that the magnetization in the SiO_2-Fe_2O_3 films is easy, nonlinear, and saturating with increasing fields applied in the film plane in both opposing directions. The hysteresis in the magnetization-field loop at 5 K is considerably wider compared to that at room temperature and the coercive field becomes comparable to those observed earlier. In several cases earlier, composites containing iron oxide had to be annealed

markedly after their synthesis in order to properly crystallize the material and, concurrently, achieve appreciable coercive field even at low measurement temperatures. For instance, Popovici *et al*.[51] observed coercivities exceeding 20 kOe at room temperature after annealing a Fe_2O_3-SiO_2 sample at 1100 ºC, whereas lower annealing temperatures did not provide sufficient degree of crystallization and accompanying significant coercivity.

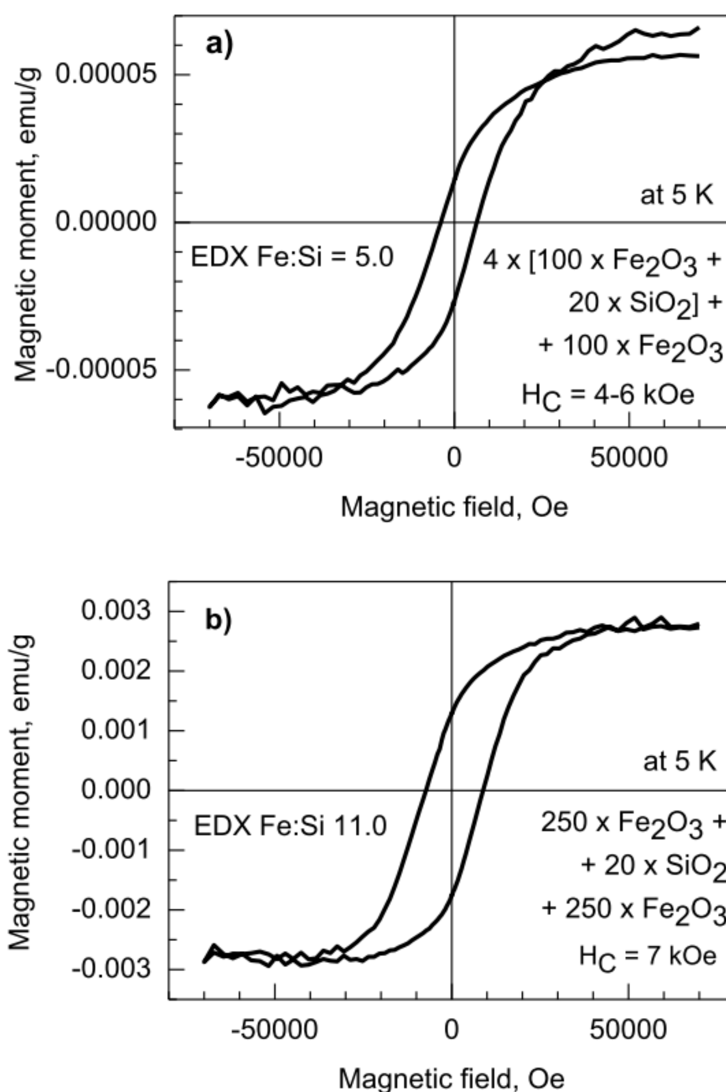

Figure 7. Magnetization-field curves measured at 5 K from a) periodical Fe_2O_3-SiO_2 nanolaminate and b) Fe_2O_3-SiO_2-Fe_2O_3 triple layer grown using ALD cycle sequences and with Fe:Si atomic ratios described by labels.

One approach has been to grow oriented ε-Fe_2O_3 layers by laser ablation at 700-900 ^oC to the thickness of 50 nm on monocrystalline ferrite substrates, as reported by Thai *et al*.[39] In these films, coercivity reaching 2 kOe was measured at 350 K. Yet in another study conducted by Balaev *et al*.[43] ε-Fe_2O_3 particles of about 5-10 nm in diameter were incorporated in composites with porous silica gel as the matrix, and calcined at 900 ^oC. Coercive fields in the range of 6-12 kOe could be achieved in magnetization-field loops, when measured at 300 K. Dubrovskyi *et al*.[40] have described the effect of the ε-Fe_2O_3 particle size to the magnetic response. In their study, ε-Fe_2O_3 particles were impregnated in silica pores by wet chemical synthesis from iron sulphate solution, and heat treated at 900 ^oC for 4 h afterwards. Upon that procedure, measurable amounts of ε-Fe_2O_3 particles with diameters in the range of 5-10 nm were produced, demonstrating coercivities within 5-6 kOe. Thus, the reference data seem to imply that high-temperature processing of Fe_2O_3-SiO_2 nanocomposites has been a pre-requisite to effective room-temperature magnetic polarization and memory effects. In the present paper, however, appreciable magnetic polarization has been achieved in the as-deposited Fe_2O_3-SiO_2 multilayer structures containing ε-Fe_2O_3 nanocrystallites.

According to the knowledge published to date, ε-Fe_2O_3 is a phase which can display complex magnetic properties. At ~ 490 K, ε-Fe_2O_3 changes from a paramagnetic state to an ordered, supposedly canted, antiferromagnetic state. With decreasing temperature, the coercivity of ε-Fe_2O_3 rapidly increases and reaches ~20 000 Oe (2 T) at room temperature and a maximum of ~22 000 Oe (2.2 T) at 200 K. Below 200 K the coercivity has been seen to decrease drastically, reaching zero at ~100 K. Below that, the coercivity recovers and strenghtens up to 5000 Oe (0.5 T) at 2 K.[40] In our samples, the coercivity measured at room temperature was much smaller that that expected for ε-Fe_2O_3. The coercivity was close to zero in the laminate

and about 700 Oe for the Fe_2O_3-SiO_2-Fe_2O_3 trilayer structure. As mentioned above, the deformed shape of the hysteresis loop of the trilayer at room temperature might indicate existence of more than one phase with different coercivity in the films. It is to be noted, that even if the XRD results allowed one to consider the formation of ε-Fe_2O_3 as the dominant phase in some samples, formation and co-existence of additional hematite phase can not be excluded and multiphase character of the nanocrystalline material is therefore still possible. Different phases would all contribute to the physical properties of the phase mixture. In this regard, Kant *et al.*[52] have synthesized stable α-Fe_2O_3 particles with dimensions ranging from 13 to 63 nm, and also measured relatively moderate coercivity values, ~6000 Oe at 10 K and ~27 Oe at 300 K. Therefore the magnetization in such nanolaminates and nanocrystalline oxides can easily vary along with small variations in the phase composition comprising different polymorphs of iron oxide.

C. Electrical behavior

Resistive switching behavior was recorded and found to be the most well defined in the SiO_2-Fe_2O_3 nanolaminate grown using the ALD cycle sequence of 4 × [75 × Fe_2O_3 + 50 × SiO_2] + 75 × Fe_2O_3 (Fig. 8, topmost panel). The ratio between the high and low resistance states was significant, extending over an order of magnitude in the conventional resistive switching measurements.

It is noteworthy, that Fe_2O_3 films have less frequently been considered as candidates for memristor media, likely due to their strongly polycrystalline nature and accompanying inferior insulating characteristics. Nevertheless, for instance in a study devoted to the ALD of

relatively smooth, uniform, and finely grained Fe_2O_3,[15] resistive switching was studied and observed. Current and resistivity values in the high resistance state could be tuned by varying the maximum voltage used for breaking conductive channels (filaments) during resetting the high resistivity. In the present study, however, the Fe_2O_3 films alone occurred too conductive and did not allow switching with reliable distinction between low and high resistance states.

Silicon oxide has been studied as one of the most promising switching medium. In a study on co-sputtering of silicon-rich silicon dioxide films,[53] conductive pathways formed were supposedly not continuous, but rather chains of partially separated silicon nanoinclusions in a highly substoichiometric oxide matrix. These SiO_x-based devices differed, at that time, from most of the other materials studied in that diffusion of metallic ions was not involved in the formation of the conductive paths.[53] In the present study, however, the as-deposited SiO_2 reference films did not exhibit appreciable switching characteristics, which was likely due to the impurities existing in the films.

In a reliably switching medium the difference between the low and high resistivity states should be at least an order of magnitude, which, in the present study, was observed in the case of the ALD cycle sequence of $4 \times [75 \times Fe_2O_3 + 50 \times SiO_2] + 75 \times Fe_2O_3$ (Fig. **8**, a). In these measurements, rectangular sampling voltage pulses were applied to the electrodes on the dielectric layer, with the pulse amplitude increasing within the sequence of pulses. At the increasing voltage pulses, currents were recorded, forming current-voltage envelope curves until the transition (switching) to the low resistance state (SET) and back to the high resistance state (RESET). However, alternatively to the conventional envelope curves, currents were registered at low-reading voltages of 0.1 V after passing each sequential

sampling voltage pulses. In this case, the measured current values were even more clearly determined by the two resistivity states than in the conventional measurements. Thus, exploitation of the low-reading voltages provided two clearly defined plateaus of current values which were recorded before and after the sequential SET and RESET transitions (Fig. 8, the 2nd panel). In this way, current-voltage loops (current memory map) with pronounced squareness were formed by the applied voltages with a distinct memory window between the high and low current states. This measurement method has become useful especially in such cases where the material possesses rather high conduction currents already in the virgin, supposedly high resitivity, state before the formation of the low resistivity state and, therefore, in the conventional measurements exhibits too small ratios between the high and low resistance states. The method has been used earlier to study the performance of some other resistively switching oxides, such as Ta_2O_5-TiO_2-Ta_2O_5 or ZrO_2-Co_3O_4,[54] and Nb_2O_5-SiO_2 nanolaminates[55] grown by ALD.

In order to evaluate capacitive behavior in addition to the direct currents through the dielectric stacks, differential capacitances were measured at a frequency of 500 kHz, also between sampling bias voltage pulses (Fig. 8). Admittance parameters were recorded along with sweeping the sampling bias voltage. Conductance, G, and capacitance, C, maps over low-reading voltage sampling were recorded, applying a parallel admittance model.[56] In order to obtain the memory maps for G and C, return-to-zero voltage pulse sequences were used. Thereby positive voltage pulses of 1 ms duration were applied while the sample was in its high resistance state. After each sampling voltage pulse, the voltage was returned to 0 V and the admittance-derived conductance and capacitance values, were recorded at 0 V bias on ac signal only. The amplitude of the sampling voltage pulse was increased linearly until the transition from the high resistance state to the low resistance state occurred, and thereafter

correspondingly decreased until the transition back to the high resistance state. The plots of capacitance, C (Fig. 8, c) and conductance, G (Fig. 8, d) as functions of the voltage, which can also be termed as the programming voltage in this case, thus constituted the corresponding memory maps.

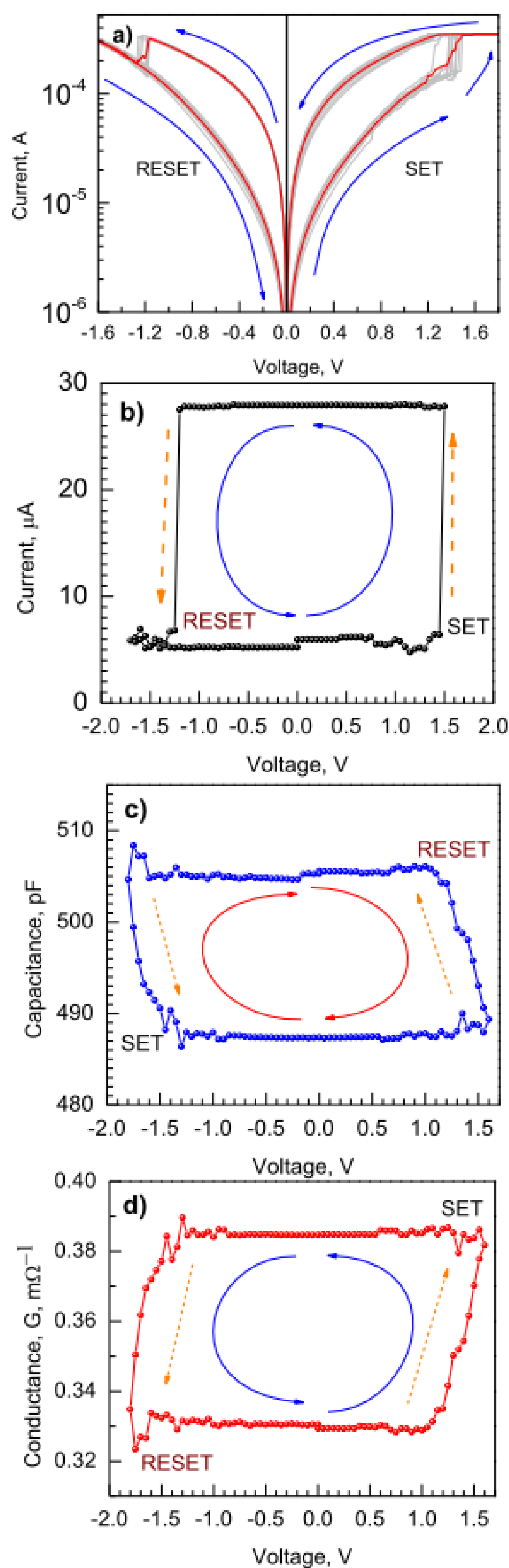

Figure 8. Current-voltage loops measured a) in the conventional resistive switching mode, b) small signal current-voltage memory map, c) small signal capacitance memory map, and d) small signal conductance memory map (bottom panel) against sampling voltage pulses applied on 30 nm thick SiO_2-Fe_2O_3 nanolaminate deposited with a cycle sequence of 4 × [75 × Fe_2O_3 + 50 × SiO_2] + 75 × Fe_2O_3].

Analogous measurements were carried out on a Fe_2O_3-SiO_2-Fe_2O_3 triple-layered film grown using the ALD cycle sequence of 250 × Fe_2O_3 + 20 × SiO_2 + 250 × Fe_2O_3. This film occured rather leaky compared to the nanolaminate grown using the ALD cycle ratio of 75:50, described above. The triple-layer sample exhibited rather weakly detectable and thus less significant resistive switching performance with a low ratio between the low and high resistivity states (Figure **9**, a). In the SiO_2-Fe_2O_3 nanolaminate grown using the ALD cycle sequence of 4 × [75 × Fe_2O_3 + 50 × SiO_2] + 75 × Fe_2O_3 (Fig. **8**, a), the conducting current values measured at -1 V during the RESET pulses in low and high resistance states were 2.8 and 1.1×10^{-4} A, respectively, making the LRS to HRS ratio equal to 2.6. In the case of the triple layer (Fig. **9**, a), the corresponding values were 2.8 and 2.0×10^{-4} A, lowering the LRS to HRS ratio to 1.4.

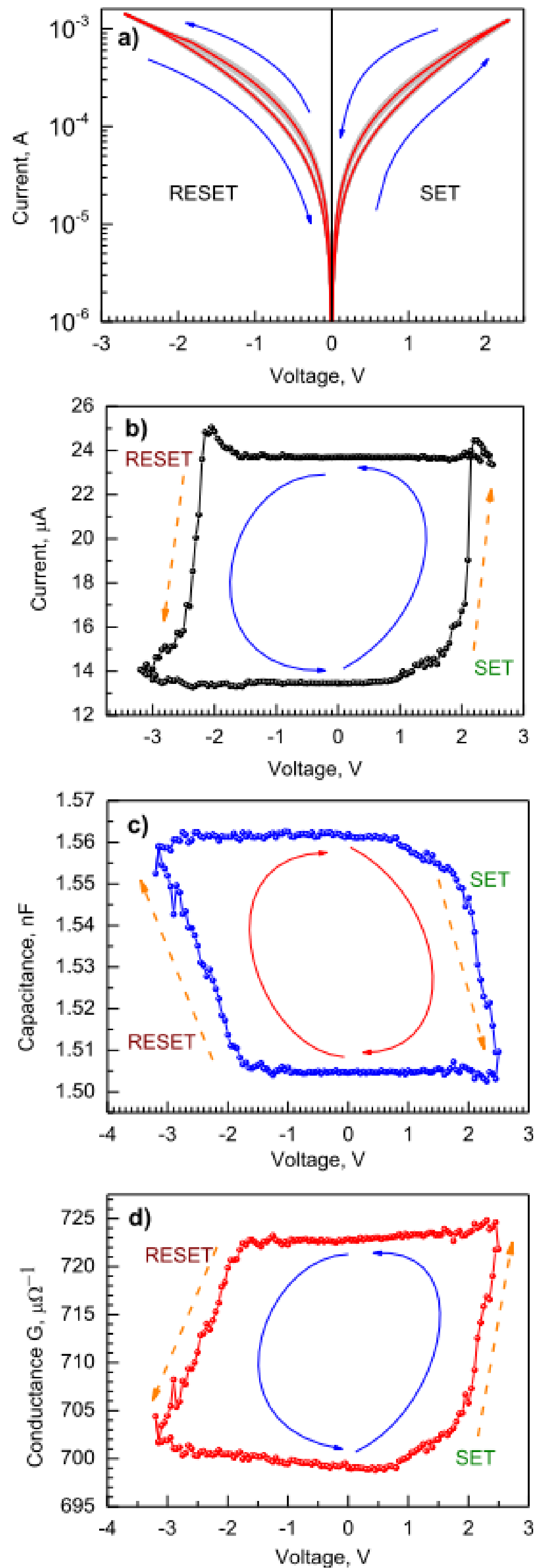

Figure 9. Current-voltage loops measured a) in the conventional resistive switching mode, b) small signal current-voltage memory map, c) small signal capacitance memory map, and d) small signal conductance memory map (bottom panel) against sampling voltage pulses applied on 50 nm thick SiO_2-Fe_2O_3 triple layer deposited with a cycle sequence of 250 × Fe_2O_3 + 20 × SiO_2 + 250 × Fe_2O_3.

Figure 9 also represents current-voltage loop measured at low-reading voltages (Fig. 9, b), as well as capacitance (Fig. 9, c), and conductance (Fig. 9, d) memory maps obtained from the admittance measurements at return-to-zero voltages, similarly to the case of the nanolaminate described above. From these one can see, that even if the conventional resistive switching property manifests itself poorly, the current measurements in the low-reading regime and admittance measurements at the return-to-zero voltage enable recording memory maps with well defined squareness and distinct differences between the low and high conductivities as well as sharp SET and RESET transition events.

IV. CONCLUSIONS

Atomic layer deposition method was exploited to grow SiO_2-Fe_2O_3 nanolaminate and mixture films on silicon and titanium nitride substrates. The elemental composition of the films could feasibly be modified by changing the ratio of successive ALD cycles for the SiO_2 and Fe_2O_3 component oxides. The crystal growth of Fe_2O_3 was initiated and intensified with the thickness of Fe_2O_3 layers in the SiO_2-Fe_2O_3 films. Along with the increment in the relative content of iron oxide and its crystallization, nonlinear and saturative magnetization in the films was detected at room temperature and enhanced at 5 K. The Fe_2O_3 layers tended to crystallize in the metastable orthorhombic ε-Fe_2O_3 phase, although some contribution of hematite to the phase composition could not be excluded.

Response of the films to the external electric fields was examined. Resistive switching performance with a pronounced window between the low and high resistivity states was recorded in the structures grown using proper ratios between SiO_2 and Fe_2O_3 growth cycles.

Admittance measurements in small-signal regime allowed one to enhance the distinction between the low and high resistance states as well as the squareness of the memory maps.

Among the structures examined, the nanolaminate grown using the ALD cycle sequence of 4 × [75 × Fe_2O_3 + 50 × SiO_2] + 75 × Fe_2O_3 was the one exhibiting clear responses to both magnetic and electric fields. The film consisted of approximately 4.4 nm thick Fe_2O_3 and 5.9 nm thick SiO_2 layers, was nanocrystalline, possibly comprising orthorhombic ε-Fe_2O_3 phase, and demonstrated saturative and nonlinear magnetization with rather narrow hysteresis at room temperature, as well as resistive switching behavior with the most prominent distinction between low and high resistivity states.

The study has demonstrated that Fe_2O_3 films, which are deposited alternately with SiO_2 films in multilayered structures, can resemble ferromagnetic nanocrystalline materials, and the electronic leakage currents may in certain extents become suppressed by controlling the contribution from the wide band-gap SiO_2. The latter also enables the appearance of resistive switching in the multilayers. In relatively leaky materials, application of small-signal measurements still ensure recording of distinct and defined memory performance. With further, more detailed parametrization and scale-up of the process in the future, one may seek the effect of electrical conductivity on magnetization and vice versa, that is, to identify a coupling effect between conductivity and magnetic polarization.

ACKNOWLEDGEMENTS

The study was partially supported by the Finnish Centre of Excellence in Atomic Layer Deposition (284623), Spanish Ministry of Economy and Competitiveness and the FEDER program (TEC2017-84321-C4-2-R), the European Regional Development Fund project "Emerging orders in quantum and nanomaterials" (TK134), and Estonian Research Agency (PRG4 and PRG753).

References:

[1] M. Tadic, V. Kusigerski, D. Markovic, I. Milosevic, and V. Spasojevic, *Mater. Lett.* **63**, 1054 (2009).

[2] P. L. Zhu, F. Xue, Z. Liu, Y. L. Fan, Z. M. Jiang, and X. J. Yang, *J. Appl. Phys.* **106**, 043907 (2009).

[3] A. Teleki, M. Suter, P. R. Kidambi, O. Ergeneman, F. Krumeich, B. J. Nelson, and S. E. Pratsinis, *Chem. Mater.* **21**, 2094 (2009).

[4] D. Ortega, J.S. Garitaonandia, M. Ramírez-del-Solar, C. Barrera-Solano, and M. Domínguez, *J. Non-Cryst. Solids,* **354**, 5213 (2008).

[5] C. Păcurariu, E.-A. Tăculescu, R. Ianoşa, O. Marinică, C.-V. Mihali, and V. Socoliuc, *Ceram. Int.,* **41**(1), 1079 (2015).

[6] C.-K. Huang, C.-H. Hou, C.-C. Chen, Y.-L. Tsai, L.-M. Chang, H.-S. Wei, K.-H. Hsieh, and C.-H. Chan, *Nanotechnology,* **19**, 055701 (2008).

[7] Y. P. He, S. Q. Wang, C. R. Li, Y. M. Miao, Z. Y. Wu, and B. S. Zou, *J. Phys. D: Appl. Phys*. **38**, 1342 (2005).

[8] N. R. Murphy, C. V. Ramana, L. Sun, J. G. Jones, and J. T. Grant, *J. Alloys Compd.* **708**, 947 (2017).

[9] X. Zhang, Y. Niu, Y. Li, Y. Li, and J. Zhao, *J. Solid State Chem.* **211**, 69 (2014).

[10] W. D. Chemelewski, N. T. Hahn, and C. B. Mullins, *J. Phys. Chem. C,* **116**, 5255 (2012).

[11] H. Jiang, X. Y. Li, R. Chen, X. L. Shao, J. H Yoon, X. Hu, C. S. Hwang, and J. Zhao, *Sci. Rep.* **6**, 22216 (2016).

[12] L. Liu, D. Yu, W. Ma, B. Chen, F. Zhang, B. Gao, and J. Kang, *Jpn. J. Appl. Phys.* **54**, 021802 (2015).

[13] J. Yao, Z. Sun, L. Zhong, D. Natelson, and J. M. Tour, *Nano Lett.* **10**, 4105 (2010).

[14] X. Yan, Z. Zhou, B. Ding, J. Zhao, and Y. Zhang, *J. Mater. Chem. C*, **5**, 2259 (2017).

[15] S. Porro, K. Bejtka, A. Jasmin, M. Fontana, G. Milano, A. Chiolerio, C. F. Pirri, and C. Ricciardi, *Nanotechnology,* **29**, 495201 (2018).

[16] Y.-F. Chang, T.-C. Chang, and C.-Y. Chang, *J. Appl. Phys.* **110**, 053703 (2011).

[17] Y.-F. Chang, Y.-T. Tsai, G.-W. Chang, Y.-E. Syu, Y.-H. Tai, and T.-C. Chang, *ECS J. Solid State Sci. Technol.* **1**, Q91 (2012).

[18] S. Ren, G. Zhu, J. Xie, J. Bu, H. Qin, and J. Hu, *J. Phys.: Condens. Matter* **28**, 056001 (2016).

[19] S. Ren, H. Qin, J. Bu, G. Zhu, J. Xie, and J. Hu, *Appl. Phys. Lett.* **107**, 062404 (2015).

[20] M.-C. Kao, H.-Z. Chen, S.-L. Young, K.-H. Chen, J.-L. Chiang, and J.-B. Shi, *Materials* **10**, 1327 (2017).

[21] R. Matero, S. Haukka, and M. Tuominen, *ECS Transact.* **13**, 453 (2008).

[22] Y. Tomczak, K. Knapas, S. Haukka, M. Kemell, M. Heikkilä, M. Ceccato, M. Leskelä, and M. Ritala, *Chem. Mater.* **24**, 3859 (2012).

[23] A. Tanskanen, O. Mustonen, and M. Karppinen, *APL Mater.* **5**, 056104 (2017).

[24] T. Suntola, *Thin Solid Films,* **216**, 84 (1992).

[25] R. A. Waldo, Microbeam Analysis, (San Francisco Press, San Francisco, CA, 1988), p. 310.

[26] J. Jokinen, J. Keinonen, P. Tikkanen, A. Kuronen, T. Ahlgren, and K. Nordlund, *Nucl. Instrum. Methods Phys. Res. B,* **119**, 533 (1996).

[27] G. Vignaud and Alain Gibaud, *J. Appl. Crystallography*, **52**, 201 (2019).

[28] N. Doebelin and R. Kleeberg, *J. Appl. Crystallography*, **48**, 1573 (2015).

[29] D. Spiga, A. Mirone, G. Pareschi, R. Canestrari, V. Cotroneo, C. Ferrari, C. Ferrero, L. Lazzarini, and D. Vernani,. *Proc. SPIE 6266, Space Telescopes and Instrumentation II: Ultraviolet to Gamma Ray,* 626616 (13 June 2006),

[30] S. Sintonen, S. Ali, O. M. E. Ylivaara, R. L. Puurunen, and H. Lipsanen, *J. Vac. Sci. Technol. A*, **32**, 01A111 (2014).

[31] J. M. Jensen, A. B. Oelkers, R. Toivola, D. C. Johnson, J. W. Elam, and S. M. George, *Chem. Mater.* **14**, 2276 (2002).

[32] J. Lee and S Park, *J. Korean Phys. Soc.* **69**, 789 (2016).

[33] L. Machala, J. Tuček, and R. Zbořil, *Chem. Mater.* **23**, 3255 (2011).

[34] J.-G. Li, G. Fornasieri, A. Bleuzen, M. Gich, A. Gloter, F. Bouquet, and M. Impéror-Clerc, *Small,* **12**, 5981 (2016).

[35] Y. Masubuchi, Y. Sato, A. Sawada, T. Motohashi, H. Kiyono, and S. Kikkawa, *J. Eur. Ceram. Soc.* **31**, 2459 (2011).

[36] K. Nomura and H. Reuther, *J. Radioanal. Nucl. Chem.* **287**, 341 (2011).

[37] L. Kubíčková, P. Brázda, M. Veverka, O. Kaman, V. Herynek, M. Vosmanská, P. Dvořák, K. Bernášek, J. Kohout, *J. Magn. Magn. Mater*. **480**, 154 (2019).

[38] J. Tuček, R. Zbořil, A. Namai, S. Ohkoshi, ε -Fe_2O_3: *Chem. Mater.* **22**, 6483 (2010).

[39] T. M. N. Thai, D. T. Nguyen, N.-S. Lee, J.-S. Rhyee, J. Song, and H.-J. Kim, *J. Appl. Phys.* **120**, 185304 (2016).

[40] A. A. Dubrovskiy, D. A. Balaev, K. A. Shaykhutdinov, O. A. Bayukov, O. N. Pletnev, S. S. Yakushkin, G. A. Bukhtiyarova, and O. N. Martyanov, *J. Appl. Phys.* **118**, 213901 (2015).

[41] M. Gich, A. Roig, C. Frontera, E. Molins, J. Sort, M. Popovici, G. Chouteau, D. Martín y Marero, and J. Nogués, *J. Appl. Phys.* **98**, 044307 (2005).

[42] A. Namai, M. Yoshikiyo, K. Yamada, S. Sakurai, T. Goto, T. Yoshida, T. M. M. Makajima, T. Suemoto, H. Tokoro, and S. Ohkoshi, *Nature Comm.* **3**, 1035 (2012).

[43] D. A. Balaev, I. S. Poperechny, A. A. Krasikov, K. A. Shaikhutdinov, A. A. Dubrovskiy, S. I. Popkov, A. D. Balaev, S. S. Yakushkin, G. A. Bukhtiyarova, O. N. Martyanov, and Yu. L. Raikher, *J. Appl. Phys.* **117,** 063908 (2015).

[44] J. Kohout, P. Brázda, K. Závěta, D. Kubániová, T. Kmječ, L. Kubíčková, M. Klementová, E. Šantavá, and A. Lančok, *J. Appl. Phys.* **117**, 17D505 (2015).

[45] I. Ahamed, R. Pathak, R. Skomski, and A. Kashyap, *AIP Adv.* **8**, 055815 (2018).

[46] J.A. Sans, V. Monteseguro, G. Garbarino, M. Gich, V. Cerantola, V. Cuartero, M. Monte, T. Irifune, A. Muñoz, and C. Popescu, *Nature Comm.* **9**, 4554 (2018).

[47] Y. El Mendili, J.-F. Bardeau, N. Randrianantoandro, J.-M. Greneche, and F. Grasset, *Sci. Technol. Adv. Mater.* **17**, 597 (2016).

[48] C. Dejoie, P. Sciau, W. Li, L. Noé, A. Mehta, K. Chen, H. Luo, M. Kunz, N. Tamura, and Z. Liu, *Sci. Rep.* **4**, 4941 (2014).

[49] M. Gich, C. Frontera, A. Roig, J. Fontcuberta, E. Molins, N. Bellido, Ch. Simon, and C. Fleta, *Nanotechnology,* **17**, 687 (2006).

[50] V. N. Nikolić, M. Tadić, M. Panjan, L. Kopanja, N. Cvjetićanin, and V. Spasojević, *Ceram. Int.* **43**, 3147 (2017).

[51] M. Popovici, M. Gich, D. Nižňanský, A. Roig, C. Savii, L. Casas, E. Molins, K. Zaveta, C. Enache, J. Sort, S. de Brion, G. Chouteau, and J. Nogués, *Chem Mater.* **16**, 5542 (2004).

[52] R. Kant, D. Kumar, and V. Dutta, *RSC Adv.* **5**, 52945 (2015).

[53] A. Mehonic, S. Cueff, M. Wojdak, S. Hudziak, O. Jambois, C. Labbé, B. Garrido, R. Rizk, A. J. Kenyon, *J. Appl. Phys.* **111**, 074507 (2012).

[54] S. Dueñas, H. Castán, K. Kukli, M. Mikkor, K. Kalam, T. Arroval, and A. Tamm, *ECS Transact.* **85**, 201 (2018).

[55] K. Kukli, M. Kemell, M. J. Heikkilä, H. Castán, S. Dueñas, K. Mizohata, M. Ritala, M. Leskelä, *Nanotechnol.* **31**, 195713 (2020).

[56] S. Dueñas, H. Castán, H. García, Ó. G. Ossorio, L. A. Domínguez, and E. Miranda, *IEEE Electron Dev. Lett.* **38**, 1216 (2017).

Table I. List of Fe_2O_3-SiO_2 films grown to the thicknesses and possessing iron to silicon elemental ratios measured by energy dispersive X-ray spectrometry (EDX).

ALD growth cycle sequences	Thickness	Fe:Si ratio
500 × Fe_2O_3; a reference iron oxide film	28 nm	
250 × Fe_2O_3 + 20 × SiO_2 + 250 × Fe_2O_3	50 nm	11:1
4 × [100 × Fe_2O_3 + 20 × SiO_2] + 100 × Fe_2O_3	47 nm	5:1
4 × [75 × Fe_2O_3 + 50 × SiO_2] + 75 × Fe_2O_3	37 nm	2:1
10 × [25 × Fe_2O_3 + 2 × SiO_2] + 25 × Fe_2O_3	48 nm	6:1
10 × [25 × SiO_2 + 4 × Fe_2O_3] + 25 × SiO_2	44 nm	0.7:1

Captions to figures

Figure 1.

Measured and fitted X-ray reflection patterns from SiO_2-Fe_2O_3 nanolaminate film grown using ALD cycle sequences indicated by the labels (left column) and schematic representation of the nanolaminate structures with layer thicknesses, d, mass densities, ρ, and roughnesses, σ, as fitting results (right column). In both panels a) and b) of the left column, every other data point is omitted for the sake of clarity.

Figure 2.

Transmission electron microscopy images of Fe_2O_3-SiO_2 nanolaminate films grown on SiO_2/Si substrates (a) and d)), Si substrates covered by a TiN layer (b) and e)), and aluminum foil (c) and f)). The corresponding growth cycle sequences are indicated on the panels in the upper row. The layers of distinct chemical composition constituting the film stacks are labeled correspondingly.

Figure **3.**

Grazing incidence X-ray diffractograms from a) 28 nm thick Fe_2O_3 film, b) 50 nm thick Fe_2O_3 film embedding a 2-3 nm thick SiO_2 interlayer, and c) a nanolaminate film after annealing at 800 ^{o}C in air. Experimental and fitted difractograms are represented by bold gray and solid black curves, respectively. Reflexes above the noise level are designated as those belonging to the Fe_2O_3 polymorphs and indicated by the corresponding labels for the epsilon-phase in top and middle panels and hematite in bottom panel.

Figure **4**.

Grazing incidence X-ray diffractograms from as-deposited Fe_2O_3 films mixed or laminated with SiO_2 with molar Fe:Si ratios (EDX), indicated by the labels. For the description of the growth cycle sequences, see Table **I**

Figure **5**.

Scanning electron microscopy images from the surfaces of Fe_2O_3-SiO_2 films as-deposited using cycle sequences indicated by the labels.

Figure 6.

Room-temperature magnetization curves measured from periodical Fe_2O_3-SiO_2 nanolaminate (a) and Fe_2O_3-SiO_2-Fe_2O_3 triple layer (b) grown using ALD cycle sequences and with Fe:Si atomic ratio described by the labels.

Figure 7.

Magnetization-field curves measured at 5 K from a) periodical Fe_2O_3-SiO_2 nanolaminate and b) Fe_2O_3-SiO_2-Fe_2O_3 triple layer grown using ALD cycle sequences and with Fe:Si atomic ratios described by labels.

Figure **8.**

Current-voltage loops measured a) in the conventional resistive switching mode, b) small signal current-voltage memory map, c) small signal capacitance memory map, and d) small signal conductance memory map (bottom panel) against sampling voltage pulses applied on 30 nm thick SiO_2-Fe_2O_3 nanolaminate deposited with a cycle sequence of $4 \times [75 \times Fe_2O_3 + 50 \times SiO_2] + 75 \times Fe_2O_3]$.

Figure **9.**

Current-voltage loops measured a) in the conventional resistive switching mode, b) small signal current-voltage memory map, c) small signal capacitance memory map, and d) small signal conductance memory map (bottom panel) against sampling voltage pulses applied on 50 nm thick SiO_2-Fe_2O_3 triple layer deposited with a cycle sequence of $250 \times Fe_2O_3 + 20 \times SiO_2 + 250 \times Fe_2O_3$.